



Emergent Spatial Patterns of Excitatory and Inhibitory Synaptic Strengths Drive Somatotopic Representational Discontinuities and their Plasticity in a Computational Model of Primary Sensory Cortical Area 3b

OPEN ACCESS

Edited by:

Florentin Wörgötter,
University Goettingen, Germany

Reviewed by:

Gaute T. Einevoll,
Norwegian University of Life Sciences,
Norway

Nicolas P. Rougier,
Institute for Research in Computer
Science and Automation (INRIA
Bordeaux), France

Hubert R. Dinse,
Ruhr-University Bochum, Germany

*Correspondence:

Kamil A. Grajski
kgrajski@nurosci.com

Received: 12 April 2016

Accepted: 29 June 2016

Published: 25 July 2016

Citation:

Grajski KA (2016) Emergent Spatial Patterns of Excitatory and Inhibitory Synaptic Strengths Drive Somatotopic Representational Discontinuities and their Plasticity in a Computational Model of Primary Sensory Cortical Area 3b. *Front. Comput. Neurosci.* 10:72. doi: 10.3389/fncom.2016.00072

Kamil A. Grajski*

NuroSci, LLC., West Palm Beach, FL, USA

Mechanisms underlying the emergence and plasticity of representational discontinuities in the mammalian primary somatosensory cortical representation of the hand are investigated in a computational model. The model consists of an input lattice organized as a three-digit hand forward-connected to a lattice of cortical columns each of which contains a paired excitatory and inhibitory cell. Excitatory *and* inhibitory synaptic plasticity of feedforward *and* lateral connection weights is implemented as a simple covariance rule and competitive normalization. Receptive field properties are computed independently for excitatory and inhibitory cells and compared within and across columns. Within digit representational zones intracolumnar excitatory and inhibitory receptive field extents are concentric, single-digit, small, and unimodal. Exclusively in representational boundary-adjacent zones, intracolumnar excitatory and inhibitory receptive field properties *diverge*: excitatory cell receptive fields are single-digit, small, and unimodal; and the paired inhibitory cell receptive fields are bimodal, double-digit, and large. In simulated syndactyly (webbed fingers), boundary-adjacent intracolumnar receptive field properties reorganize to within-representation type; divergent properties are *reacquired* following syndactyly release. This study generates testable hypotheses for assessment of cortical laminar-dependent receptive field properties and plasticity within and between cortical representational zones. For computational studies, present results suggest that concurrent excitatory and inhibitory plasticity may underlie novel emergent properties.

Keywords: area 3b, somatosensory cortex, syndactyly, inhibitory synaptic plasticity, somatotopy, neuroplasticity

INTRODUCTION

Representational discontinuity is a striking feature of the normal somatotopic map of the hand in primary sensory cortical area 3b in adult owl monkeys (Merzenich et al., 1978; Merzenich et al., 1987; Kaas et al., 1979; Sur, 1980; Sur et al., 1980; Merzenich et al., 1990; Recanzone et al., 1992). Excitatory receptive fields empirically derived in cortical layer IV samples spaced as closely as 50–100 μm can have profoundly different extents on the skin surface. Within representational zones excitatory receptive fields typically display a remarkable continuity: small to medium-sized, unimodal excitatory receptive fields overlap in smooth progressions over the skin surface. Between representational zones “step changes” were reported including those between adjacent digits, between glabrous and hairy skin, between palmar pads and digits, and between the face and digits, among others.

The purpose of this computational study is to explain—at the level of spatial patterns of adapted synaptic weights in excitatory and inhibitory model neurons—the emergence and reorganization of somatotopic representational continuities and discontinuities. The model system is that of area 3b in adult owl monkeys and its reorganization subject to digital syndactyly and release (Allard et al., 1991).

This study shares features in common with previous studies. First, of interest is the contribution of the interplay between excitation and inhibition (e.g., lateral or surround inhibition) in determining individual and collective excitatory receptive field properties. Second the basic model unit is that of a cortical column that consists of excitatory and inhibitory cell(s) with characteristic interconnectivity, including mutual excitatory-excitatory cell connections and recurrent inhibition.

This study is unique in two ways. First, all synaptic types are adapted subject to a simple covariance rule. These include synapses between sensory afferents to cortical excitatory cells, lateral cortical excitatory to excitatory cells, lateral cortical excitatory to inhibitory cells, and lateral cortical inhibitory to excitatory cells. Adaptation of the excitatory to excitatory connection type is Hebbian-like: spiking rate activity in the former is facilitative of changes in spiking rate in the latter. The same holds for the excitatory to inhibitory connection type. Since the inhibitory to excitatory connection type is facilitative of *not* firing action potentials in the latter due to action potential firing by the former the adaptation rule is not strictly Hebbian, but is covariance-driven. Other than an initial local random weight distribution, there is no external overlay of synaptic patterning, for example, to effect details of lateral inhibition. Second, the study reports the results of separate analyses of individual and collective receptive field properties observed in the population of excitatory cells (excitatory receptive fields) *and* in the population of inhibitory cells (inhibitory receptive fields). This enables a more detailed understanding particularly of the role of inhibition in cortical somatotopy. Spatial patterns of synaptic strengths are observed that appear not to conform simply to lateral inhibition (at least in its most simplistic stereotypical form).

The study concludes that in the present neural network model, representational continuities and discontinuities and their reorganization are a consequence of the emergence of

characteristic spatial patterns of synaptic weights in both excitatory and inhibitory neural populations. The study illustrates these spatial patterns and tracks their evolution in a simulated three-digit somatotopic map from initial random conditions, to a baseline refinement, through simulated digital syndactyly, and release from syndactyly.

The effects typically attributed to and which result as a consequence of lateral inhibition are shown to be an emergent property of neural networks whose connection weights are subject to a simple covariance adaptation rule. These may represent a novel emergent neural mechanism contributing to cortical somatotopy.

MATERIALS AND METHODS

Model

The model consists of a pair of forward connected two-dimensional lattices each containing a 45×45 array of nodes. An input layer (S) node consists of a single “input unit” with exclusively ascending connections to its corresponding topographically centered 7×7 neighborhood of cortical layer (C) nodes. There is no skin surface model and no mechanoreceptor-specific model. Individual input layer afferents are experimentally activated as ON or OFF (with additive noise). The activity on these afferents is considered to model individual and groups of fast conduction velocity low-threshold cutaneous mechanoreceptors positioned in glabrous skin (Zimmerman et al., 2014).

A cortical layer node consists of an excitatory (E) and inhibitory (I) cell pair. These are interpreted as a lumped representation of a cortical column. Cortical layer E-cells are the exclusive target of S layer ascending connections. A cortical layer E-cell makes collateral excitatory connections with itself, with a corresponding topographically centered 7×7 neighborhood of E-cells, and with a neighborhood of I-cells. A C layer I-cell makes collateral inhibitory connections with a corresponding topographically centered 7×7 neighborhood of E-cells. See **Tables 1A–G** (formatted as proposed in Nordlie et al., 2009). Neither axonal nor other spatial delay is modeled. Normalization of input weights enforces planar boundary conditions. Control experiments confirm that for the present settings of lateral connection spatial divergence and network sizes $N > 20$ edge effects are confined to the regions one to three nodes in from each edge. The C layer consists of 2025 columns (4050 cells) and $\sim 400,000$ synapses.

The model neuron is an RC-time constant membrane potential (v_i) subject to depolarization and hyperpolarization through weighted input connections. The S layer input unit is, in addition, driven by an external ON/OFF stimulus. Average spiking rate (r_i) for the neurons and input units are modeled by passing the corresponding membrane potential (v_i) through a sigmoidal compression function. See **Table 1D**.

Synapses (connection weights) are initially assigned values from a uniform distribution. These are subsequently adapted according to exponential decay, a simple covariance rule, and normalization. Weight adaptation (plasticity) is controlled by

TABLE 1A | Model Summary.

Populations	Three: excitatory (E), inhibitory (I), external excitatory input (S).
Topology	Cartesian grids for cortical layer (C) and external input layer (S)
Connectivity	Rectangular mask; excitatory self-connection: yes; inhibitory self-connection: no; multiple connections: no.
Neuron model	Lumped RC model, average spiking rate (r_i) proportional to membrane potential (v_i) via sigmoidal function, $g(v)$.
Synapse model	Connection weight ($w_{i,j} = w_{post,pre}$)
Plasticity	Connection weight is a linear combination of exponential decay term and a term proportional to the covariance of presynaptic and postsynaptic average firing rates, and postsynaptically normalized to a population type dependent “resource” level.
Input	Fixed-size, fixed-duration, and fixed-magnitude (with additive random noise) rectangular masks presented in random positions within or across external input layer partitions to model three independent digits of a hand.
Measurements	Membrane potential; average spike rate; excitatory and inhibitory receptive fields.

TABLE 1B | Populations.

Name	Elements	Size
E	Cortical column excitatory element	$N_E = 2025$ (e.g., 45×45 cortical layer grid)
I	Cortical column inhibitory element	$N_I = 2025$ (e.g., 45×45 cortical layer grid)
S	Excitatory external input element	$N_S = 2025$ (e.g., 45×45 input layer grid)

TABLE 1C | Connectivity.

Name	Source	Target	Pattern
EE	E	E	Centered local $M \times M$ grid ($M = 7$); random initial weights; no delay
IE	E	I	Centered local $M \times M$ grid ($M = 7$); random initial weights; no delay
EI	I	E	Centered local $M \times M$ grid ($M = 7$); random initial weights; no delay
ES	S	E	Centered local $M \times M$ grid ($M = 7$); random initial weights; no delay

an external ON or OFF signal. When ON, connection weight adaptation occurs at each time step Δt in the numerical integration. See **Table 1E**. When ON, connection weights are normalized at the end of each stimulus presentation trial. See **Table 1F**.

Model Inputs and Experimental Protocol

The present study is organized as an “experimental” track consisting of three phases (baseline, syndactyly, and syndactyly release) and a corresponding “control” track (baseline, syndactyly control, and syndactyly release control). Each phase consists of a set of 15 cycles. Each cycle consists of a set of 0.350 s duration trials. Model inputs are presented and model outputs measured during each such trial. See **Table 1F**.

Phase I “baseline refinement” is the simulation that models the emergence and maintenance of somatotopy from random initial conditions. A single baseline refinement cycle consists of stimulating all possible patches of a fixed size one at a time per trial *while respecting digit “boundaries.”* The number of 7×7 patches in a 45×45 baseline network is 351 per digit (total 1053/cycle). The baseline refinement phase consists of 15 cycles (15,795 trials). Weight adaptation is ON during baseline refinement. A receptive field map is derived after each cycle. See **Table 1G**. During the receptive field mapping procedure weight adaptation is OFF.

Phase II “syndactyly refinement” is the simulation that models the response of a baseline refined network to simulated digital syndactyly. The driving stimuli are spatially localized, correlated inputs on layer S. A single syndactyly refinement cycle consists of stimulating all possible patches of a fixed size one at a time per trial *while respecting the D2-D3 boundary, but ignoring the D1-D2 boundary.* The number of 7×7 patches in a 45×45 syndactyly network is 351 for D3 and 936 for the syndactyly D1+2 (total 1287/cycle). The syndactyly refinement phase consists of 15 cycles (19,305 trials). Weight adaptation is ON during syndactyly cycles. A receptive field map is derived after each cycle. During the receptive field mapping procedure weight adaptation is OFF.

Phase III “syndactyly release” repeats Phase I, but uses the syndactyly network as its starting point. Weight adaptation is ON during syndactyly release. A receptive field map is derived after each cycle. During the receptive field mapping procedure weight adaptation is OFF.

The Experimental track evolves a single network of fixed size and fixed input patch size through Phase I (baseline refinement), Phase II (syndactyly) and Phase III (syndactyly release). On the Experimental track, digits 1 and 2 are the “experimental” digits; D3 provides within-network control.

The Control track starts with the Experimental Phase I baseline refined network and subjects it to two additional complete baseline refinement runs. In this protocol D3 undergoes the same total number of stimulation trials overall on both the Control and Experimental tracks. Similarly, all areas of digits 1 and 2 (sufficiently distant from the D1–D2 border) undergo the same number of stimulation trials.

Figure 1 shows the per trial stimulation count for baseline and syndactyly trials normalized to the same magnitude scale for the network used throughout this study. This protocol controls for the effects of overall stimulation count.

Model Outputs

Simulated receptive field mapping is a two-step process. A Receptive Field Probe trial is run one at a time once for each layer S node ($N = 2025$) and the cortical layer E and I cell activity stored. See **Table 1F**. Next, the recorded data is post-processed to calculate receptive field response magnitude, area (extent), orientation and position, for each cortical layer E cell and I cell. See **Table 1G**.

TABLE 1D | Lumped Neuron and Input Unit Models.

Type	Description
Cortical column excitatory element	$v_i^E(t+1) = \alpha_m v_i^E(t) + \sum_j r_j^S(t) w_{ij}^{ES}(t) + \sum_j r_j^E(t) w_{ij}^{EE}(t) - \sum_j r_j^I(t) w_{ij}^{EI}(t) + \epsilon(t),$ $\alpha_m = (1 - h/\tau_m), h = 0.001, \tau_m = 0.025, \epsilon(t) \text{ i.i.d. uniform distribution of values between } \pm 0.01$
Cortical column inhibitory element	$v_i^I(t+1) = \alpha_m v_i^I(t) + \sum_j r_j^E(t) w_{ij}^{IE}(t) + \epsilon(t)$
Excitatory input layer element	$v_i^S(t+1) = \alpha_m v_i^S(t) + \delta_i^S(t) + \epsilon(t),$ $\delta_i^S - \text{S unit } i \text{ output OFF (=0) or ON (=1)}$
Spiking, r	$r = g(v) = \frac{1}{2} (1 + \tanh[\beta_m (v - \frac{1}{2})]), \beta_m = 4.0$
Numerical	Fourth Order Runge-Kutta numerical integration with 1 ms step size: $\Delta t = h = 0.001$.

TABLE 1E | Synapse Model.

Initialization	All initial weight values uniform i.i.d. Postsynaptic normalization. Planar boundary conditions. No spatial preconditioning.
Adaptation	$w_{ij}(t+1) = \alpha_W w_{ij}(t) + \beta_W(t) r_i(t) r_j(t),$ $\alpha_W = (1 - h/\tau_W), \tau_W = 100\tau_m,$ $\beta_W(T+1) = \alpha_\beta \beta_W(T), \alpha_\beta = 0.99, \beta_W(T=0) = (0.00025), T \text{ defined below (Table 1F)}$
Postsynaptic Normalization	Excitatory: $\frac{1}{N_i} \sum_j w_{ij} = R_W = 2.0$ Inhibitory: $\frac{1}{N_i} \sum_j w_{ij} = R_W = 1.0$

TABLE 1F | Input.

Type	Description
Baseline Organization	Model three digits of the hand as non-overlapping 45×15 subarrays of 45×45 external input grid.
Baseline Trial	A 350 ms trial in which a contiguous patch of S layer units of fixed-size (7×7) is set to ON with magnitude ($v = 1.0 + \epsilon(t)$) for 50 ms following a 100 ms pre-stimulus period; in each time step during stimulus presentation the input is vector normalized to magnitude 4.0; patch position is random and respects digit “boundaries”
Baseline Cycle	One cycle (T) consists of the block of trials (N_b) required to present every possible Baseline Trial once in random order.
Syndactyly Organization	Model surgical “fusion” of two digits as a 45×30 subarray of the 45×45 external input grid; the remaining 45×15 subarray serves as the “control” digit
Syndactyly Trial	For the control digit same as a Baseline Trial. For the fused digits same as Baseline Trial, but the input patch position ranges over the 45×30 subarray. Input patches delivered to both the control and fused digits respect the “boundary” between the control digit and fused digits.
Syndactyly Cycle	One cycle (T) consists of the block of trials (N_b) required to present every possible Syndactyly Trial once in random order.
Receptive Field (RF) Probe Trial	A 350 ms trial in which a single S layer unit is set to ON with magnitude ($v = 1.0 + \epsilon(t)$) for 50 ms following a 100 ms pre-stimulus period.

RESULTS

Temporal Response during Receptive Field Probe

Figure 2 shows typical receptive field probe trial activity from a single column C layer E cell and I cell. The response consists of a low latency excitatory response in the E cell and a delayed strong excitatory response in the corresponding I cell. Both excitation levels build during the early portion of stimulus presentation. The E cell subsequently undergoes strong hyperpolarization. I cell activation decays with a dominant RC-time constant characteristic. The time series shown is from a network produced by the Phase I baseline refinement protocol.

Excitatory Receptive Field Centroids

Figure 3 depicts the evolution of excitatory receptive field centroids over the course of the experimental track. The

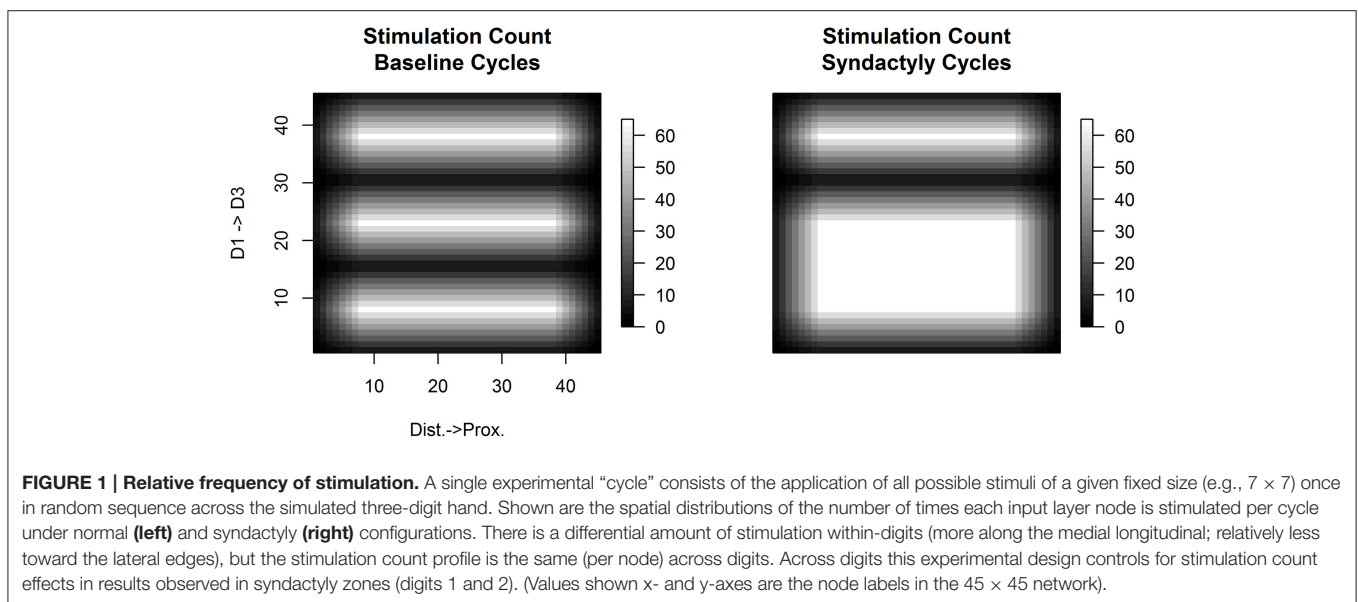
dashed lines in each panel indicate digit stimulation boundaries projected to topographically equivalent positions on the cortical lattice. Edge effects appear as expected and are limited to the extreme edges and corners of the network.

Of particular interest in this study are the boundaries between digits 1 and 2 (the experimental discontinuity) and between digits 2 and 3 (the control discontinuity). In the unrefined network the distribution of centroids is largely uniform and random. In the baseline refined network centroids cluster to either side of the digit midline. There are no centroids located on the nodes on either side of and immediately adjacent to digit boundaries (with the exception of a few nodes at network edge).

Following a single syndactyly refinement cycle the D1–D2 boundary is nearly obliterated. The border between digits 2 and 3 remains intact (with the exception of a few nodes at the network edges). Additional syndactyly refinement cycles fine-tune the centroid map.

TABLE 1G | Measurements.

Type	Description
Unit Activity	Membrane potential (v_i), average firing rate (r_i), connection weights (w_{ij})
Receptive Field	<p>Receptive field is defined as the subset of layer S nodes that drive the given cell firing rate to greater than 50% of the maximum firing rate observed in that cell across the entire set of receptive field probe trials. Receptive field response magnitude is defined as the maximum observed ratio of mean stimulus-period firing rate to mean pre-stimulus period firing rate.</p> <p>Receptive field location is defined as the maximum likelihood estimate of position over the set of layer S nodes in the receptive field (e.g., sample estimate of the mean), where each layer S node is assigned a coordinate on a uniform 2D grid. Receptive field orientation is approximated using maximum likelihood estimation (e.g., sample estimates) of the covariance matrix of the positions of the layer S nodes in the receptive field.</p> <p>For display purposes, the mean and covariance values are used as input parameters to a unimodal Gaussian distribution to generate an estimate of the receptive field extent (e.g., 50% level). Note: with such a procedure multi-peaked or discontinuous receptive fields will display as single large receptive fields so it is important to inspect and to interpret map displays accordingly.</p>



Syndactyly release cycles reverse the effects of simulated syndactyly. Following a single cycle, a D1–D2 representational boundary begins to reemerge, though there remain centroids located on nodes immediately adjacent to the boundary. The D1–D2 boundary is fully restored with additional refinement cycles. The effects observed at the edges of the D2–D3 border during syndactyly are reversed as well. Additional syndactyly release cycles produce a map of excitatory receptive field centroids indistinguishable from a baseline refined map.

Inhibitory Receptive Field Centroids

The results for inhibitory receptive field centroids are at once similar and strikingly different from those for excitatory receptive field centroids. **Figure 4** illustrates the evolution of inhibitory receptive field centroids.

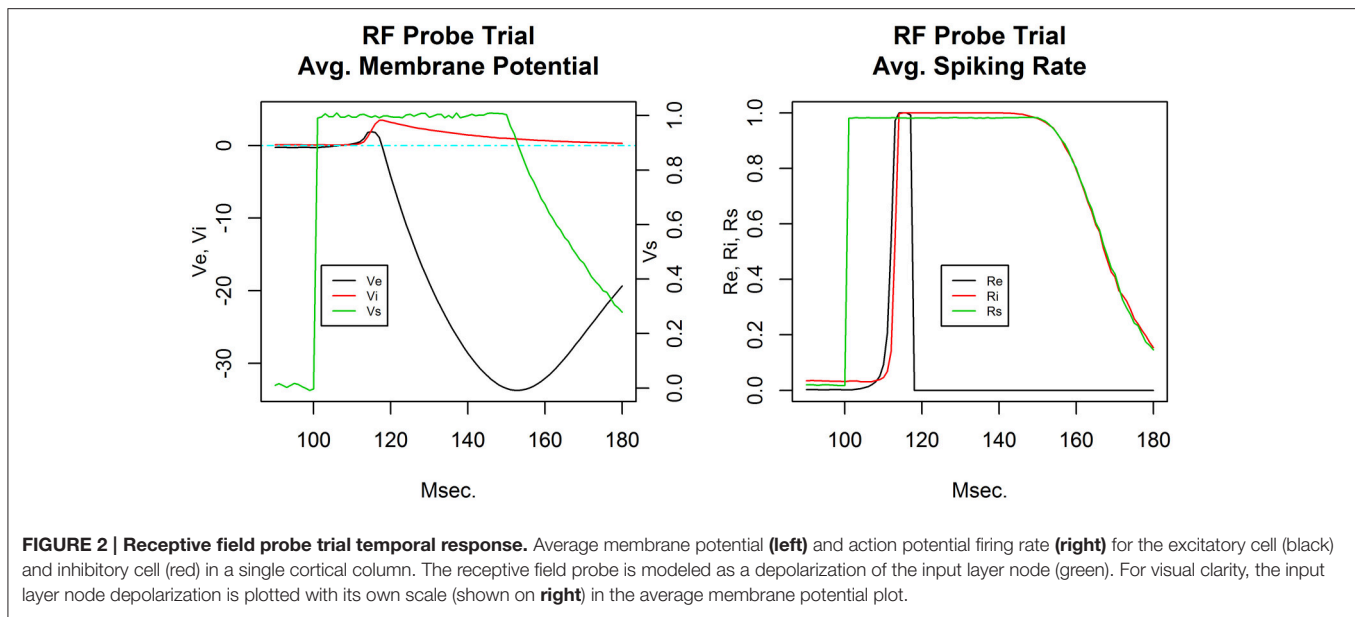
In the unrefined network the distribution of centroids is largely uniform and random. In the baseline refined network, in similar fashion to excitatory receptive fields, the inhibitory receptive field centroids cluster to either side of the digit midline. The E cell and I cell within these single cortical columns have coincident centroids.

A dramatic difference between excitatory and inhibitory receptive field centroid distributions is the observation of inhibitory receptive field centroids positioned on the nodes on either side of and immediately adjacent to digit boundaries. The E cell and I cell within these single cortical columns have divergent centroids.

Following a single syndactyly refinement cycle the D1–D2 boundary is nearly eliminated. The D2–D3 boundary remains intact. The consequence of additional syndactyly refinement cycles is a fine-tuning of the D1–D2 centroid map.

Syndactyly release cycles reverse the effects of simulated syndactyly. The border between D1–D2 begins to reemerge following a single baseline refinement cycle. Inhibitory receptive field clusters begin to migrate back toward their respective digit midlines and inhibitory receptive field centroids reappear located on the nodes on either side of and immediately adjacent to digit boundaries.

With additional syndactyly release cycles the D1–D2 boundary is fully restored. Inhibitory receptive field centroids reappear located on the nodes on either side of and immediately adjacent to D1–D2 boundary. At the D2–D3 boundary the inhibitory receptive field centroids



located on the nodes on either side persist and undergo fine-tuning. The overall result is a map of inhibitory receptive field centroids nearly indistinguishable from a baseline refined map.

Excitatory Receptive Field Extents and Overlap

Figure 5 depicts along representative fixed longitudinal recording tracks the evolution of excitatory receptive field extents and overlap. One recording track is located immediately adjacent to the D1–D2 border on the D1 side and serves as an “experimental” track. The second recording track is located along the midline of D3 and serves as a “control” track. Both tracks are selected on the basis that in the event of a strict one-to-one mapping of input layer to cortical layer these tracks would correspond to the zones indicated. The dashed lines in each panel indicate digit boundaries.

In the unrefined network, control track excitatory receptive fields are of similar though not uniform size, orientation and overlap. Experimental track excitatory receptive fields are of similar size, orientation and overlap. They are all double-digit D1, D2 in extent.

Baseline refinement yields features of normal somatotopy on both the experimental and control tracks. First, receptive fields are continuous, single-peaked, and roughly uniform in size (with possible though limited edge effects). Second, topographic order is preserved within digit representations. Third, receptive field overlap is greatest for immediately adjacent within-digit recording sites, and decreases monotonically with distance along the digit longitudinal axis. Last, representational discontinuities emerge. With the exception of a few sites at the extreme edges of the network, there are no longer any double-digit excitatory receptive fields on the experimental recording track. On the experimental track, receptive field centroids have shifted away

from the D1–D2 border and toward the D1 midline, and receptive field sizes are smaller than those on the control track.

Following a single syndactyly refinement cycle the D1–D2 boundary is nearly obliterated. All of the excitatory receptive fields recorded on the experimental track have shifted their centroid away from the D1 midline and have acquired “double-digit” receptive field extent. Other features of normal somatotopy persist on both the experimental and control tracks. The consequence of additional syndactyly refinement cycles on the experimental track is a fine-tuning and greater uniformity of excitatory receptive field size. Differences in excitatory receptive field size between extreme edge and interior on the experimental track mitigate.

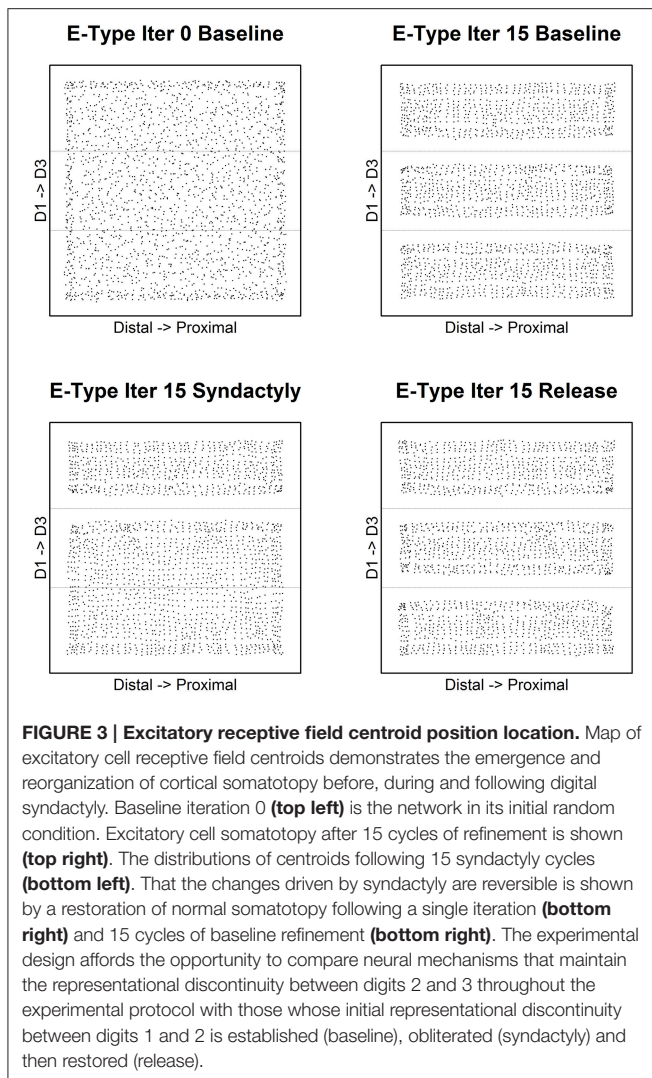
The effects of simulated syndactyly are reversible. Following a single cycle of baseline stimulation, excitatory receptive fields on the experimental track begin to migrate back in the direction of the D1 midline (not shown). Receptive field sizes, orientations and extent of overlap are more variable. Additional syndactyly release cycles result in a map of excitatory receptive field centroids indistinguishable from a baseline refined map.

Inhibitory Receptive Field Extents and Overlap

The results for inhibitory receptive field extents and overlap are at once similar and strikingly different from those for excitatory receptive field extents and overlap.

Figure 6 depicts along fixed longitudinal recording tracks the evolution of inhibitory receptive field extents and overlap. The recording tracks are the same as in **Figure 5**.

In the unrefined network, control track inhibitory receptive fields are of similar though not uniform size, orientation and overlap. Experimental track inhibitory receptive fields are

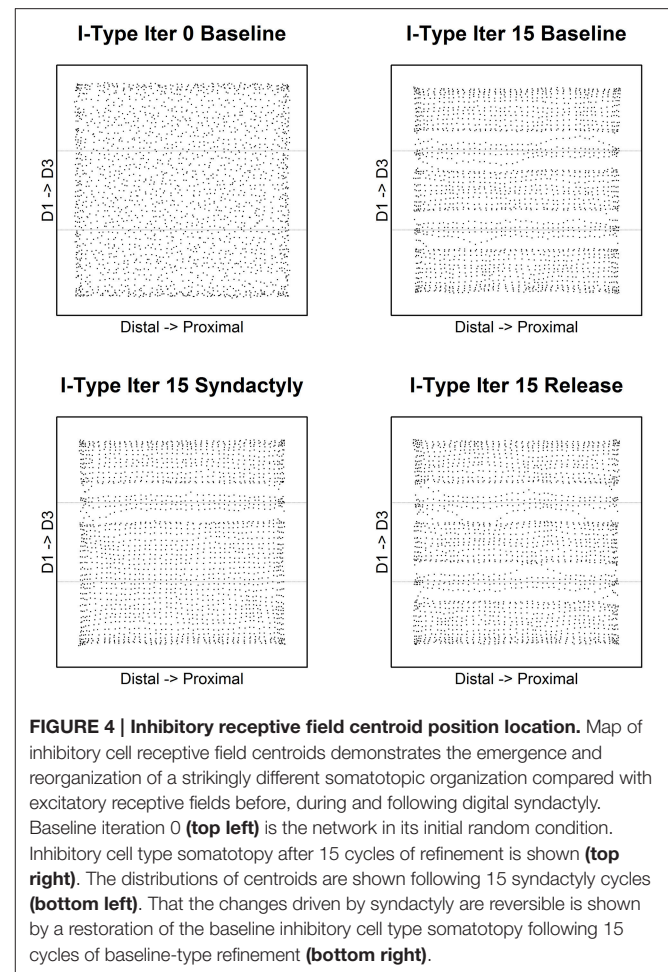


of similar size, orientation and overlap. Experimental track inhibitory receptive fields are double-digit in extent and larger than corresponding excitatory receptive fields.

Baseline refinement yields features of normal somatotopy on both the experimental and control tracks. First, receptive fields are continuous, single-peaked, and roughly uniform in size. Second, topographic order is preserved within digit representations. Last, receptive field overlap is greatest for immediately adjacent within-digit recording sites, and decreases monotonically with distance along the digit longitudinal axis.

There are differences between the control and experimental tracks. On the control track, inhibitory receptive field locations have not changed, but they are reduced in size and are single digit in extent. On the experimental track, inhibitory receptive field positions have not significantly translocated, but extent is much larger.

Comparison of the excitatory and inhibitory control tracks shows that inhibitory receptive field extent and overlap are



greater than those of excitatory receptive fields in the same cortical column.

Comparison of the excitatory and inhibitory experimental tracks reveals profound differences in receptive field extent, orientation and degree of overlap. By visual inspection, inhibitory receptive field extent is much greater, there is less or no apparent orientation, and there is greater overlap. Whereas E cell receptive fields are single-digit in extent, I cell receptive field extents are double-digit and as will be shown below bimodal. A consequence of baseline refinement is a subset of cortical columns whose E cell and I cell receptive field characteristics profoundly differ. This divergence is located exclusively along (both sides of) representational discontinuities.

Following a single syndactyly refinement cycle changes are observed in both the control and experimental tracks. On the control track, by visual inspection the single cycle syndactyly inhibitory receptive field extents appear to be more variable, with some possible effects at the network edges, compared with the baseline refined results. It is likely that the changes observed on the control track are driven by a combination of network edge effects, frequency of stimulation and the profound changes occurring on the experimental track. On the experimental track, again by visual inspection, the inhibitory

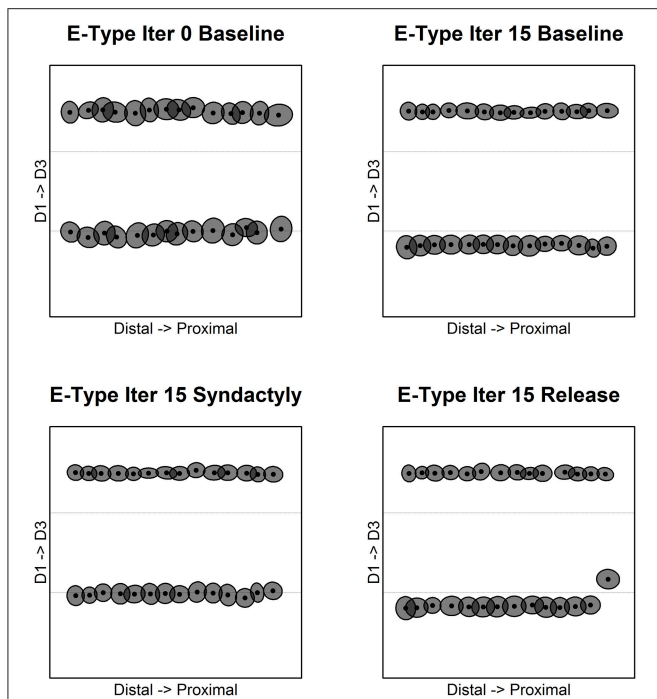


FIGURE 5 | Excitatory receptive field extents and overlap. Excitatory cell receptive fields measured along a pair of representative longitudinal recording tracks in the simulated cortical layer conform to expectations of small, overlapping receptive fields that form smooth representational progressions. Without loss of generality only every third cortical column results are shown. In each panel the upper longitudinal track is along D3 midline (row 38 of 45 in the network; row 8 in the 15 row D3 representation); the lower track is along the longitudinal axis on the D1 side of the representational border between digits 1 and 2 (row 15 of 45 in the network; row 15 in the 15 row D1 representation). Baseline evolution is shown for iteration 0 (**top left**) and after 15 cycles of refinement (**top right**). Receptive field extents and overlap are shown following 15 syndactyly cycles (**bottom left**). That the changes driven by syndactyly are reversible is shown by a restoration of somatotopy following 15 cycles of baseline refinement (**bottom right**).

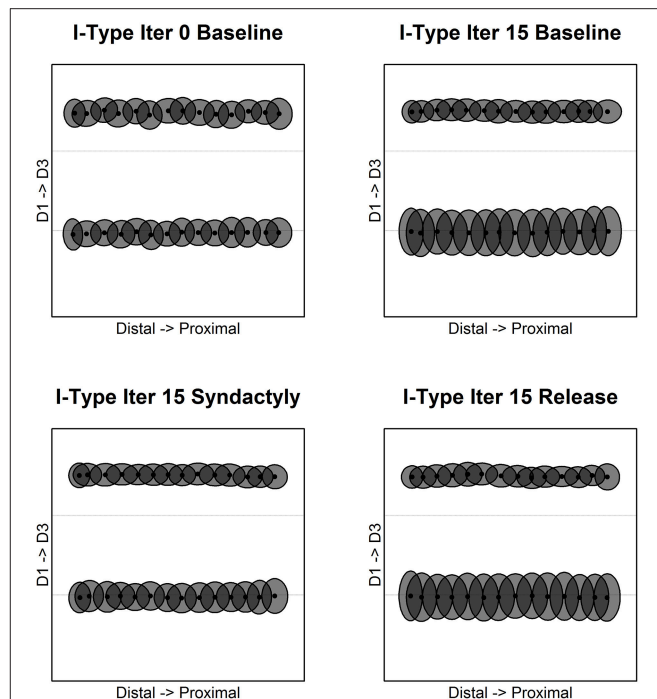


FIGURE 6 | Inhibitory receptive field extents and overlap. Inhibitory cell receptive fields measured in the same nodes as in this figure show a strikingly different organization. In each panel the upper longitudinal track is along D3 midline (row 38 of 45 in the network; row 8 in the 15 row D3 representation); the lower track is along the longitudinal axis on the D1 side of the representational border between digits 1 and 2 (row 15 of 45 in the network; row 15 in the 15 row D1 representation). Baseline evolution is shown for iteration 0 (**top left**) and after 15 cycles of refinement (**top right**). Receptive field extents and overlap are shown following 15 syndactyly cycles (**bottom left**).

receptive fields are smaller and show relatively more orientation, compared with the baseline refined results. The consequence of additional syndactyly refinement cycles on the experimental track is a further reduction in inhibitory receptive field extent and increased orientation.

Following a single post-syndactyly release cycle of normal stimulation, inhibitory receptive fields on the experimental track resemble those of a baseline refined network. Additional syndactyly release cycles result in a map of inhibitory receptive field centroids largely indistinguishable from that of a baseline refined map. The exceptions are minor in the form of a few inhibitory receptive fields whose size or orientation appear somehow “in between” that of the syndactyly refined and baseline refined network.

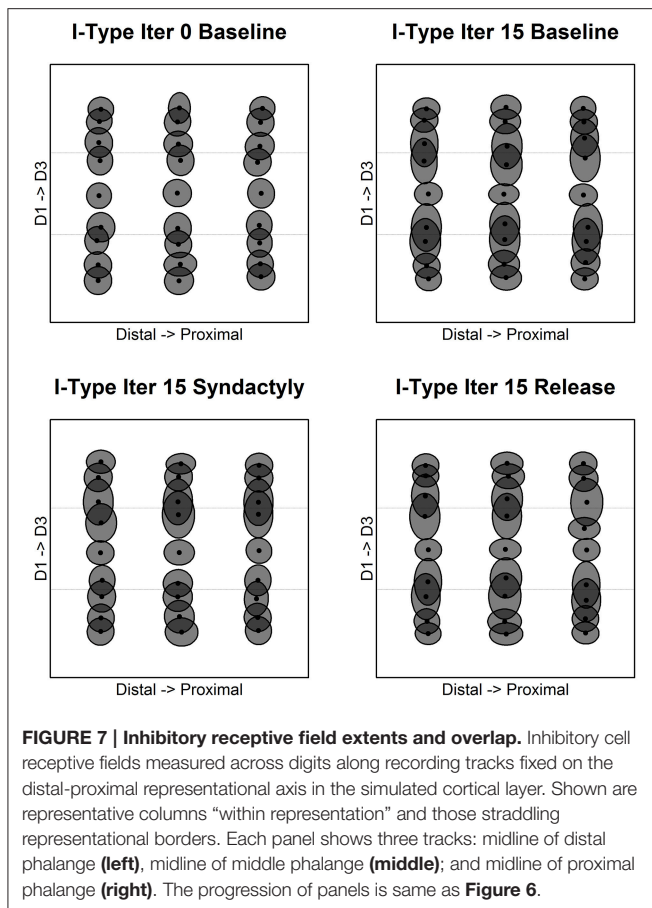
Figure 7 depicts along representative fixed cross-digit recording tracks the evolution of representative inhibitory receptive field extents and overlap. Each recording track is located in approximately the middle of the distal, mid, proximal phalange, respectively. Tracks are selected on the basis that

were there a one-to-one mapping of input layer to cortical layer these tracks would correspond exactly to the zones indicated.

Figure 8 depicts the evolution of the spatial pattern of intracolumnar excitatory and inhibitory receptive field centroids divergence over the course of the experimental track. Divergence is defined as the Euclidean distance between the E and I receptive field centroids. Assuming unit distance separation between input layer units, a divergence value >1.414 represents a shift of one unit diagonally. Divergence values are highest in the bands of columns immediately adjacent to and on both sides of representational discontinuities. *These numerical results confirm the visual observation to be shown below that in the regions near discontinuities the E cells are unimodal, single-digit and small, and the I cells are bi-modal, double-digit and large.*

Detailed Analysis of Individual Simulated Cortical Columns

Detailed analysis of individual simulated cortical columns reveals characteristic differences between columns located within a cortical representational zone and those immediately adjacent to and on either side of a cortical representational discontinuity.



Column (#333) is within the D1 representation adjacent to the D1 representational midline. **Figure 9** shows the evolution of E cell and I cell receptive field extent and response magnitude across experimental conditions. In both cases, what emerges from baseline refinement and persists through syndactyly refinement are continuous, coincident, single-digit, single-peaked receptive fields with common orientation. The inhibitory receptive field is larger in extent and lower response magnitude than the excitatory receptive field.

Figure 10 shows the evolution of E cell and I cell spatial patterns of incoming synaptic weights across experimental conditions. Each panel is a zoomed 7×7 image with its own magnitude scale to enhance contrast and to reveal fine spatial detail. The coordinates of column #333 are at center (4, 4) of each subplot. The interpretation of the data shown in each panel is that the cell positioned in the center receives inputs from itself and neighboring cortical columns. The anatomical parameters selected for this model establish the maximum number of input weights as coming from a 7×7 grid of cortical columns. Each panel shows all of the incoming weights to the cortical column located at the center. Time evolves within the figure columns from top to bottom.

The spatial pattern of input layer to excitatory cell synaptic weights following baseline refinement is a single-peaked, continuous distribution concentrated within a sub-zone slightly

offset from center. The configuration remains stable throughout syndactyly refinement. The spatial pattern of excitatory to excitatory synaptic weights is single-peaked and remains stable from baseline refinement through syndactyly refinement. Notably, following baseline refinement, the spatial pattern of inhibitory to excitatory weights is nearly uniform with little or no orientation. The range of values of the weights is wider following syndactyly, though still narrow (ratio of maximum to minimum is 1.16 in contrast to excitatory to excitatory connection type maximum to minimum ratio of 2.7). The inhibitory cell in cortical column #333 receives weighted inputs from a 7×7 grid of excitatory cells. Following baseline refinement, the spatial pattern of weights is single-peaked, through broad, continuous, and slightly offset from center away from the discontinuity between digits 2 and 3, and slightly proximal. Following syndactyly refinement, the spatial pattern remains single-peaked, continuous, but is more concentrated in a zone distal to center and slightly toward the border between digits 2 and 3.

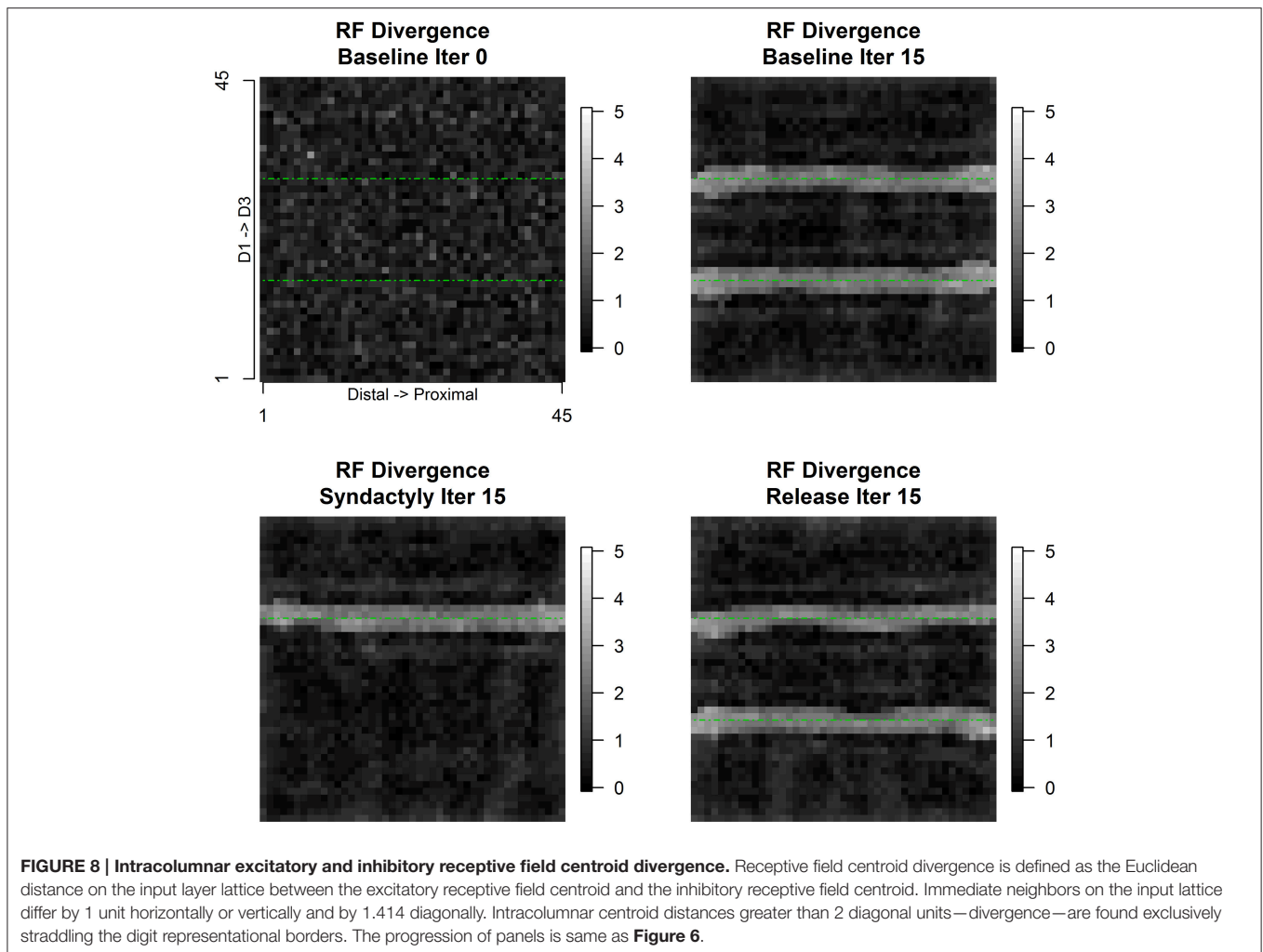
The above analysis was repeated on all applicable cortical columns with similar results. These results establish a profile of characteristic spatial patterns of incoming excitatory and inhibitory synaptic weights within cortical representational zones. The stage is set for a comparative analysis with cortical columns straddling a cortical representational discontinuity.

Cortical column (#648) lies immediately adjacent to the D1-D2 cortical representational discontinuity. **Figure 11** shows the evolution of E cell and I cell receptive field extent and response magnitude across experimental conditions. In the case of the excitatory cell, what emerges from baseline refinement and persists through syndactyly refinement is a continuous, coincident, single-digit, single-peaked receptive field. The excitatory receptive extent follows a characteristic evolution across experimental conditions: double-digit at initial random state; single-digit as a result of baseline refinement (including translocation of the receptive field centroid); and double-digit (including translocation of the receptive field centroid) as a result of syndactyly.

The inhibitory receptive field—from the same cortical column #648—undergoes a dramatically different evolution. The progression from initial conditions to a baseline refined map results in a large, double-digit receptive field. The progression from baseline refined map to a syndactyly refined map—wherein the D1-D2 representational boundary is obliterated—results in an inhibitory receptive field single-digit profile characteristic of a normal within-representational inhibitory cell. Not shown is the further result that following syndactyly release, the double-digit inhibitory receptive field characteristic is restored and is indistinguishable from that recorded at baseline refinement.

Figure 12 shows the evolution of E cell and I cell spatial patterns of incoming synaptic weights across experimental conditions for cortical column #648. The organization of **Figure 12** is the same as **Figure 10**. For every type of synapse studied there is a dramatic progression of changes across experimental conditions from initial random conditions to baseline refinement to syndactyly refinement.

The spatial pattern of input layer to excitatory cell synaptic weights undergoes shifts that are highlighted in comparison



with the position of the D1-D2 border indicated by the green line. The result of baseline refinement is a tight cluster of weights exclusive to D1 locations spanning the region between the D1 midline and the D1-D2 representational boundary. As a result of syndactyly there is a significant shift such that there is a large, single-peaked continuous pattern spanning locations on both D1-D2. The resulting distribution is indistinguishable from that of a normal baseline within-representational zone profile. Not shown is the further result that following syndactyly release refinement the baseline refined map spatial pattern is largely, if not completely, recovered.

The changes in spatial pattern of excitatory to excitatory cell synaptic weights across experimental conditions mirrors those of the sensory afferent to excitatory cells. The result of baseline refinement is a broad nearly flat distribution of weights originating from a subset of connected excitatory cells whose receptive fields, in turn, are located exclusively on D1 locations spanning the region between the D1 midline and the D1-D2 boundary. The ratio of maximum to minimum connection weight within-digit (proximal-distal axis) is $\sim 2x$, whereas the

ratio of maximum to minimum connection weight across digits is $>100x$ (in favor of D1). As a result of syndactyly there is a significant shift such that there is a large, nearly symmetric continuous pattern with contributions from excitatory cells whose receptive fields are “double-digit” from both D1 and D2, and where the ratio of maximum to minimum connection strength is $\sim 2.25x$. The resulting distribution is indistinguishable from that of a normal baseline within-representational zone profile. Following syndactyly release the baseline refined map spatial pattern is reacquired.

The spatial pattern of inhibitory to excitatory cell synaptic weights changes shares many, but not all of the features of those described for sensory afferent to excitatory, and excitatory to excitatory. The notable difference is that as a consequence of baseline refinement the excitatory cells receive inputs from inhibitory cells on both sides of the representational border. The source of inhibitory inputs from D2 is restricted to the two rows wide band immediately adjacent to the D1-D2 representational boundary. The spatial pattern of connection strengths is highly oriented across-digits, but nearly uniform within-digit representation.

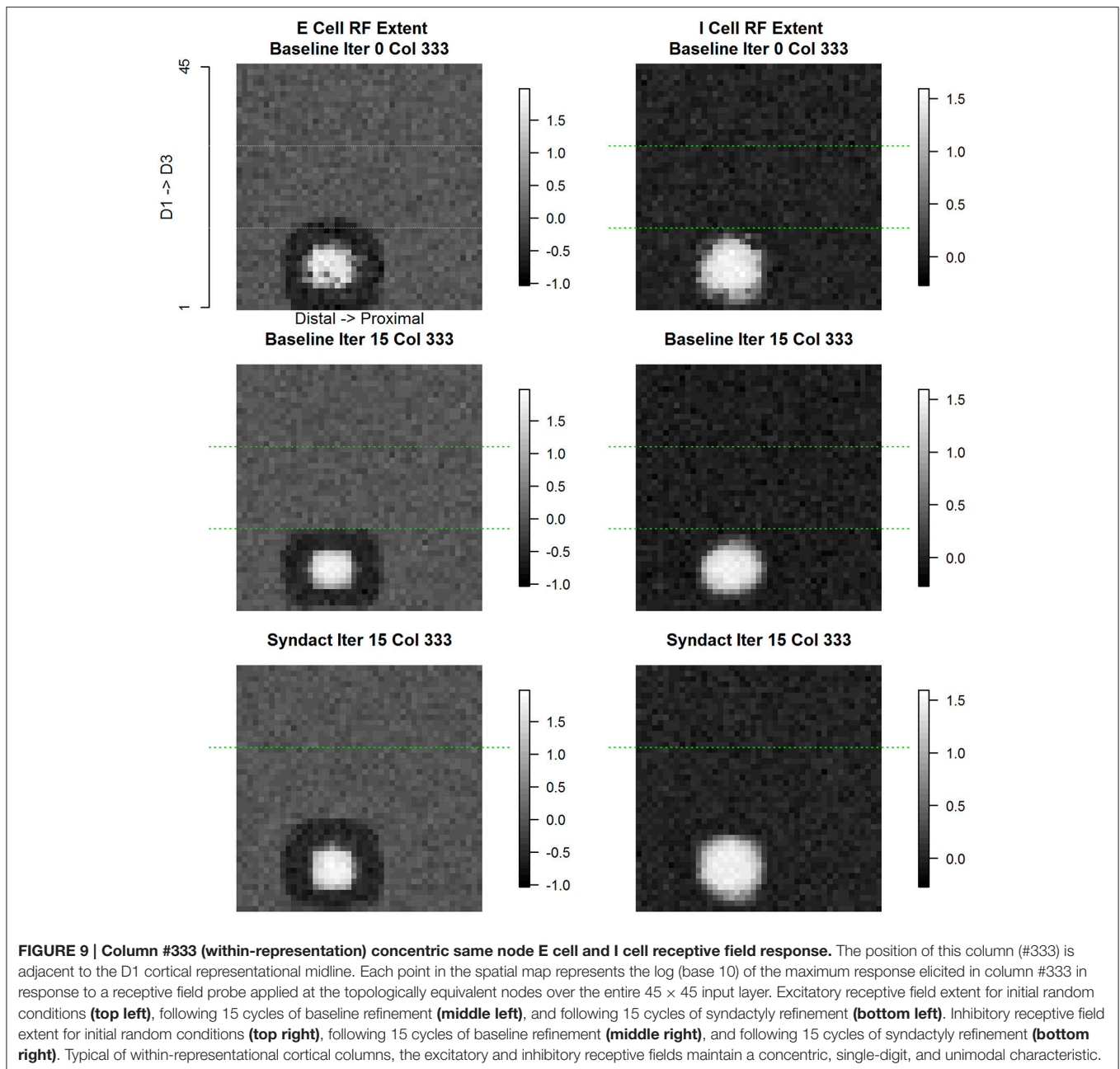


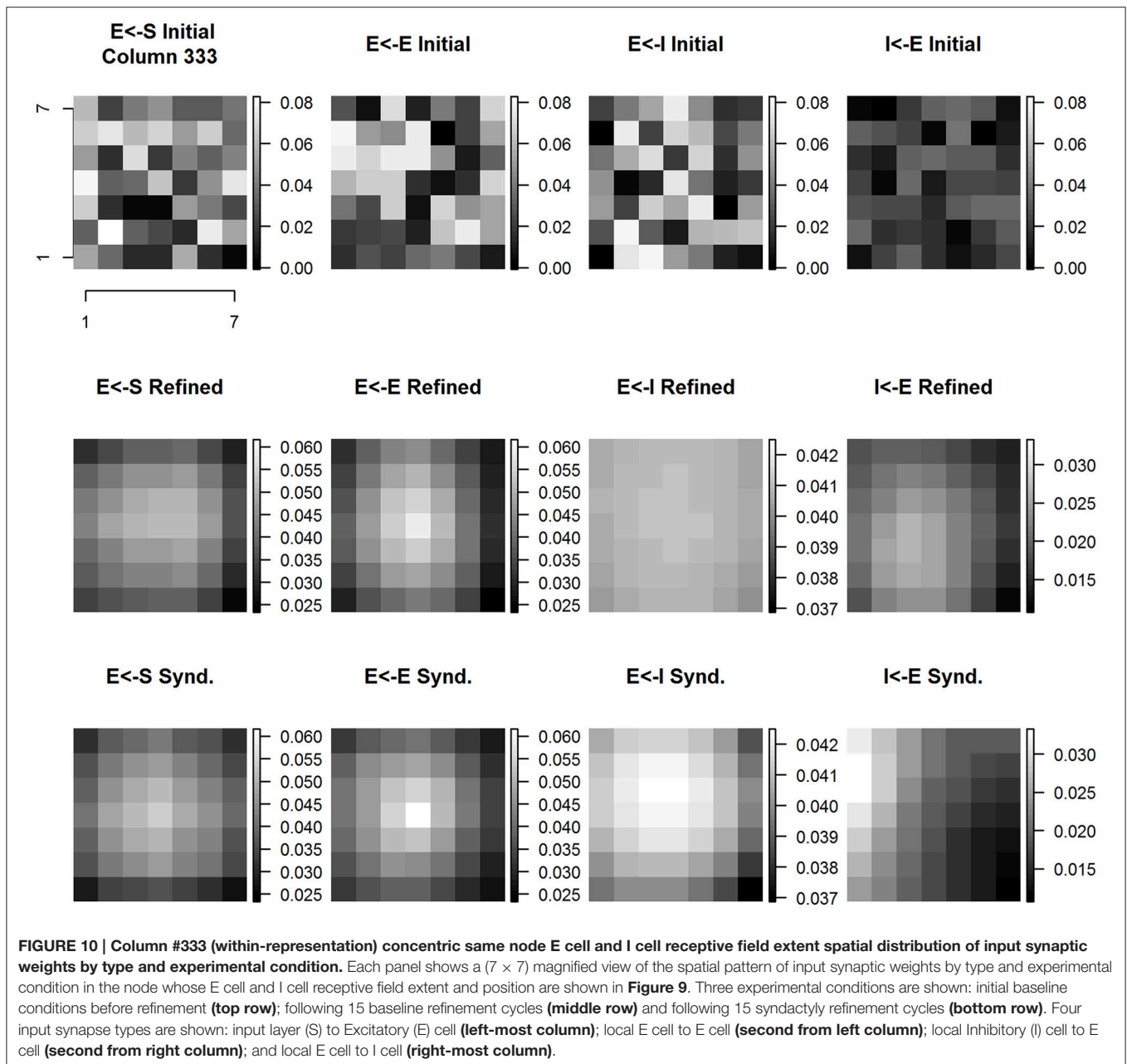
FIGURE 9 | Column #333 (within-representation) concentric same node E cell and I cell receptive field response. The position of this column (#333) is adjacent to the D1 cortical representational midline. Each point in the spatial map represents the log (base 10) of the maximum response elicited in column #333 in response to a receptive field probe applied at the topologically equivalent nodes over the entire 45×45 input layer. Excitatory receptive field extent for initial random conditions (**top left**), following 15 cycles of baseline refinement (**middle left**), and following 15 cycles of syndactyly refinement (**bottom left**). Inhibitory receptive field extent for initial random conditions (**top right**), following 15 cycles of baseline refinement (**middle right**), and following 15 cycles of syndactyly refinement (**bottom right**). Typical of within-representational cortical columns, the excitatory and inhibitory receptive fields maintain a concentric, single-digit, and unimodal characteristic.

The results are consistent with and reveal at the level of individual synaptic weight patterns the basis for the observed double-digit inhibitory receptive fields. Following syndactyly release refinement, the baseline refined map spatial pattern is reacquired.

The progression of changes across experimental conditions of the spatial pattern of excitatory to inhibitory cell synaptic weights is unique compared to those discussed above. The result of baseline refinement is a multi-peaked distribution of weights whose sources are from excitatory cells on both sides of the representational border. There is a concentration from excitatory

cells whose own receptive fields lie on the opposite side of the representational border (on D2) and with a slight distal offset. A broader, less concentrated contribution arises from excitatory cells whose own receptive fields lie on the same side (D1) of the representational border. These are shown in **Figure 12** second row, rightmost column.

The above analysis was repeated on all applicable cortical column pairs straddling a representational border with similar results. These results establish a profile of characteristic spatial patterns of incoming excitatory and inhibitory synaptic weights that contribute to cortical representational discontinuities.



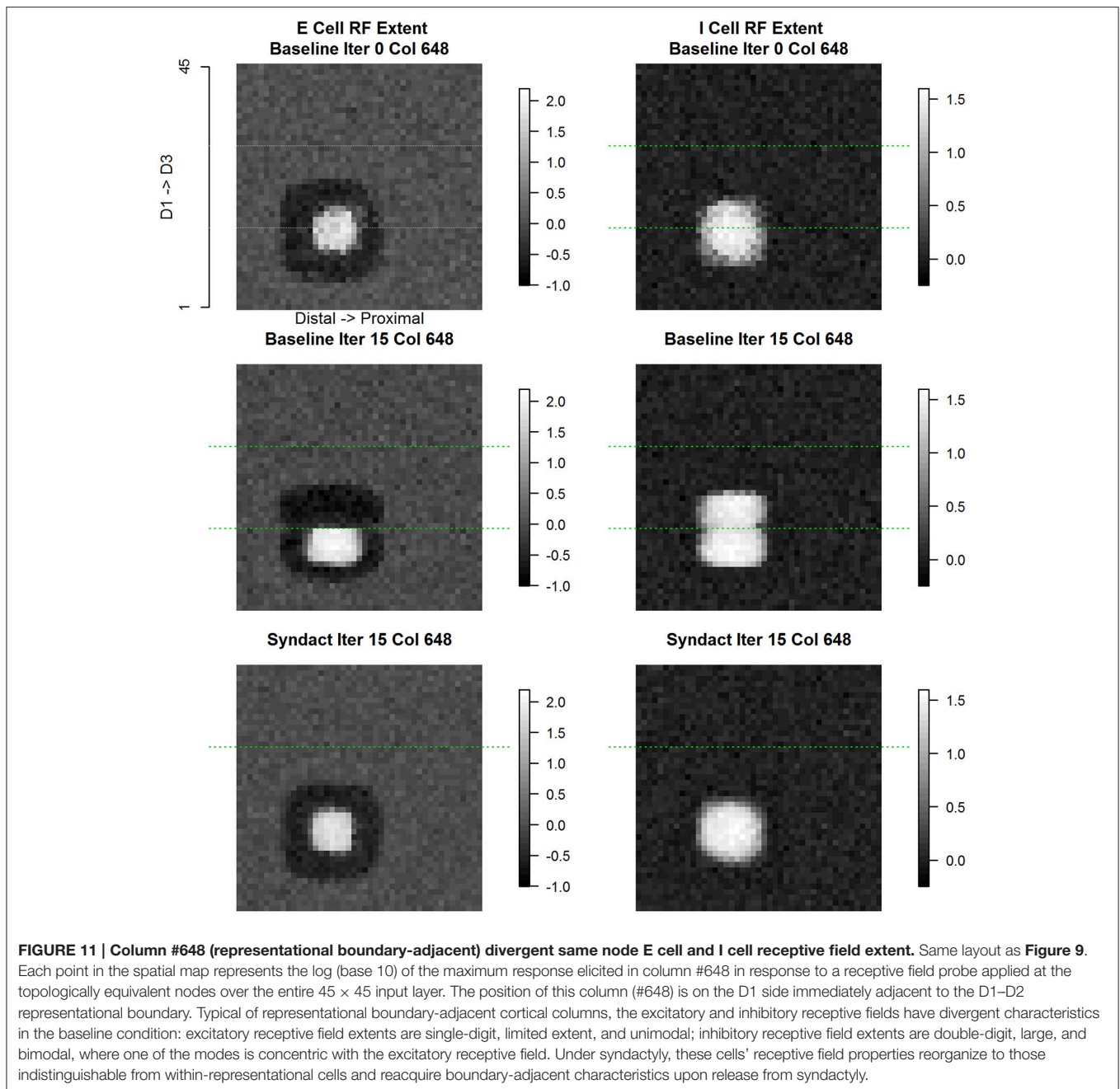
Control Experiments

Experimental Track II yields confirmatory control data (not shown) wherein the network undergoes substantially similar or nearly identical counts of stimulation but absent the syndactyly procedure. Throughout all phases, cycles and trial, the network maintains expected features of topographic organization and receptive field characteristics. Visual observation of topographic order and convergence of the network were confirmed with numerical measures of topographic order (not shown) (Goodhill and Sejnowski, 1996).

A control network was stimulated as a variation on Baseline Refinement in which the input patches ranged smoothly over the entirety of the input layer. The frequency of stimulation followed

a similar pattern to that shown in **Figure 1**. With the exception of the first few outer rings of the network every input layer node received the same maximum number of stimulations per cycle. The control experiment confirms the absence of representational discontinuities and the absence of spatial patterns of excitation and inhibition characteristic of regions adjacent and on both sides of representational discontinuities. Results are consistent with the conclusion that the observations reported in this study are unique to representational discontinuity.

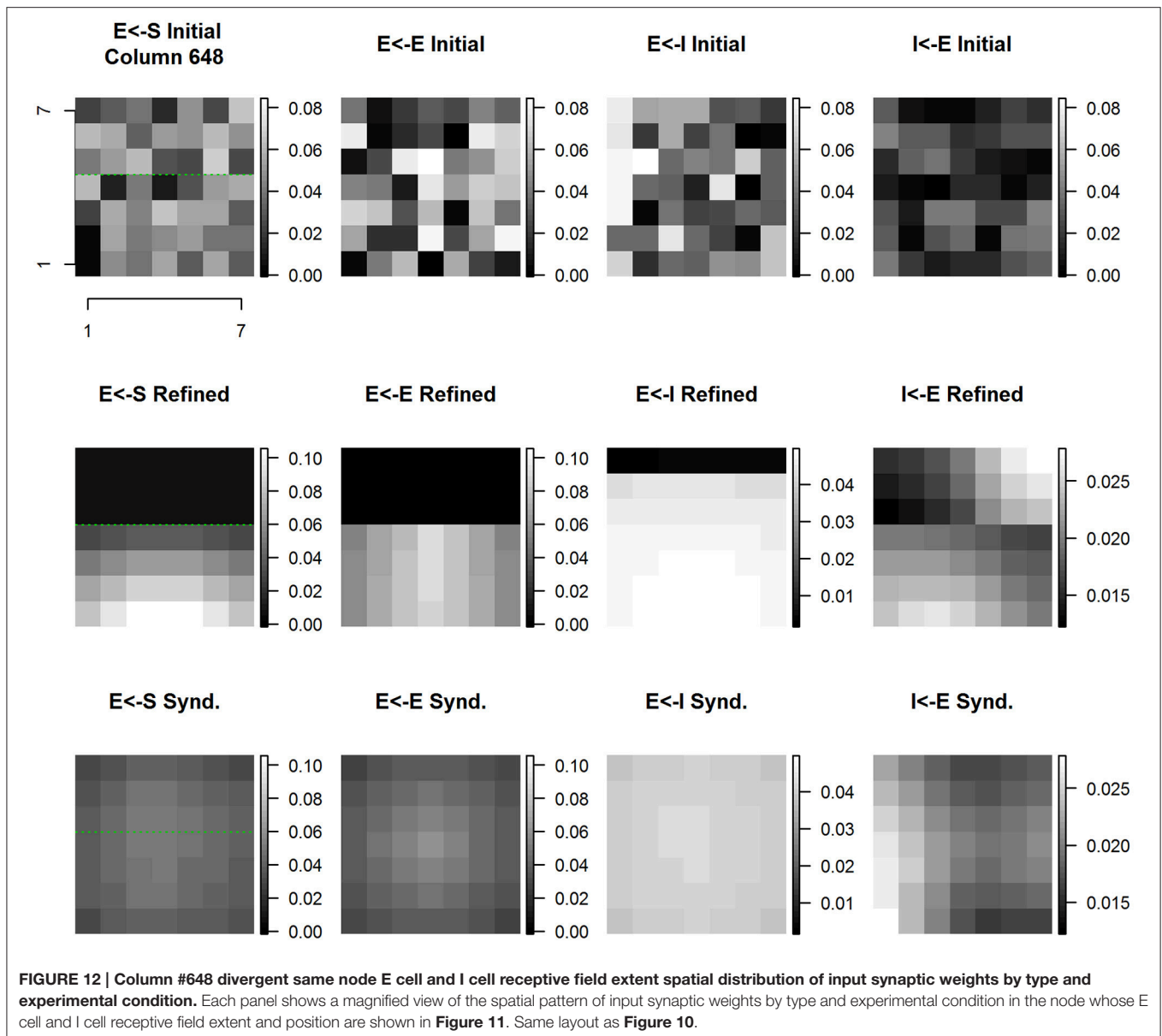
Multiple control experiments were conducted to test the hypothesis that the results obtained in this study are merely an artifact due the input stimulation pattern. In particular, during Baseline Refinement, there is a descending gradient in



stimulation count moving away from midline toward the digit border or network edge. See **Figure 1 left**. A 15×15 input pattern eliminated this gradient. With the exception of the proximal-most and distal-most edges of the network all input layer nodes received the same count of stimulations. Rerunning the entirety of this study using the 15×15 input patch yielded no obvious differences (by visual inspection and numerical measure of topographic order) from the results reported above. The study was repeated with additional parameter variations. These included: (a) a range of input patch sizes from 5×5 to 15×15 ; (b) additional cycles up to 20 to confirm convergence; (c) varying

input stimulus duration from 50 to 250 ms; (d) input stimulus magnitude [1.0, 2.0, 4.0, 8.0]; (e) varying the size of the local extent of connections from 3×3 to 4×4 , and 5×5 ; (f) repeated trials ($N = 5$) with 45×45 networks with independent random number generator seeds; and (g) repeated trials ($N = 3$) with 75×75 networks with independent random number generator seeds. The results reported above were confirmed across all of these parameter variations and network trials.

A final set of control experiments sought to characterize the width of the “band” of double-digit inhibitory cells straddling the digit representational discontinuities. In a network of size



30×30 the width of the band of double-digit inhibitory cells was confined to a single row on either side of the discontinuity for a total of two rows. In the present 45×45 case there are two rows of such cells on both sides of the discontinuity for a total of four rows. Across repeated trials with 45×45 and 75×75 networks, the first row immediately to either side of the discontinuity inhibitory cells uniformly took on the characteristic of double-digit, bi-modal, large receptive field extent. In the next unit distance row away from the discontinuity and on both sides, inhibitory cells clearly maintained a double-digit characteristic, but for cells on the D1 (D2) side the receptive field extent and response magnitude favored D1 (D2) sites. In all cases the divergent characteristic was restricted at most to the first two rows on either side of a representational discontinuity.

DISCUSSION

Summary of Results

Simulation studies with a computational model of area 3b demonstrate novel emergent properties of inhibitory cells located exclusively in zones immediately adjacent to and on either side of cortical representational discontinuities. The model consists of a lattice of cortical columns wherein a simple covariance synaptic plasticity rule is paired with competitive normalization to tune *all* of the network connection weights. These inhibitory cells' input spatial patterns of synaptic weights, and receptive field extent, orientation and overlap on the input layer differ profoundly from those observed in: (a) the paired excitatory cell in the same cortical column, though with characteristic overlap; and (b) excitatory and inhibitory cells' properties in

cortical columns located at a distance from the representational discontinuity. The stabilization of and reversible reorganization of the properties of these inhibitory cells contributes to the plasticity of simulated cortical representational discontinuity observed before, during and following release from simulated digital syndactyly between two of the digits in a simplified three-digit model of the hand. These simulations suggest that: (a) local and long-range receptive field structure and its plasticity may reflect fundamentally emergent properties of cortical neural networks of the present type; (b) where computational network connectivity is assigned *a priori*, results may mask these emergent properties; and (c) the magnitude of excitatory and inhibitory receptive field structure plasticity in and around representational discontinuities *must* be of greater magnitude—and thus may be more readily accessible to measurement by the neurophysiologist perhaps through the analysis of laminar differences—compared to within-representational zones.

Limitations and Extensions

Limitations and available extensions of the present study are in relation to variation of system parameters, certain as yet unexplored configuration which themselves may prove fruitful, and network stability conditions.

Results are reproduced and confirmed in networks obtained by systematically varying some, but not all network parameters. Parameters systematically varied include network size ($N = 15$ to $N = 45$ in steps of 5; and $N = 75$), input patch size (1×1 – 15×15), synaptic plasticity adaptation rate, number of cycles per run, input patch stimulation duration and trial length, among others. Variables not systematically varied are those relating to the anatomical spread of input node cortical layer connections, and the extent of local connectivity amongst connection types intrinsic to the cortical layer. One reason to not prioritize such analysis is that even with the present value of 7×7 local connectivity grids, the excitatory-excitatory cell connections values, for example, are observed to concentrate in sub-regions with rapid fall off to the edges. A systematic analysis could vary the local neighborhood connectivity from less than 7×7 to an all-to-all connection motif. Other limitations in the present study that could potentially be material include the use of only a single fixed input patch size in a given experiment and the presentation of only a single stimulus per trial. More complex characterizations of area 3b receptive field structure have been obtained experimentally (Dicarlo et al., 1998; DiCarlo and Johnson, 2002) and explored in a subsequent computational model (Detorakis and Rougier, 2014). With regards to such analyses, the present results beg the question as to the spatial distribution of the different observed receptive field structures with respect to representational discontinuities.

An unexplored observation in the present study is why the emergent receptive field sizes in the excitatory and inhibitory cells take on their particular observed values? What are the relative contributions of factors such as connection weight adaptation step size, input-to-cortical afferent spread, extent of local connectivity, and input patch grid size? Receptive field sizes in the present study remained within 15% average size with respect to the baseline refined network. Unexplored in the present study

is how to interpret such results with respect to the cortical and inverse cortical magnification rules. The cortical magnification rule appears to hold in that cortical magnification of input zones is roughly proportional to relative frequency of stimulation of that zone. However, with receptive field sizes held relatively constant (the primary mode of reorganization is translocation of receptive field centroids) this study does not contribute directly to the question of inverse cortical magnification.

Network stability is a consideration and by itself a potentially fruitful area for further exploration using networks of the present type (Grajski and Merzenich, 1990; Binas et al., 2014.) The conditions over which present results are reproduced are those wherein a balance is obtained between excitation and inhibition locally in the network. This is empirically determined by setting of individual connection-type resource (R) parameters to assure return to steady state following presentation of an input stimulation in each trial. While the present results are reproduced across a range of conditions, a number of pathological conditions (seizure-type activity, degenerate cortical maps) are observed under not too “distant” conditions. Such conditions include manipulating the connection weight adaptation rate, boosting or reducing the effectiveness of the excitatory-to-excitatory connections, boosting or reducing the effectiveness of excitatory-to-inhibitory, and inhibitory-to-excitatory R values, or in other cases, by introducing various combinations of connection-type silencing to simulate cortical lesion or stroke. Pathologies are observed in both temporal and spatial domains.

In a characteristic temporal pathology, the network does not return to steady state following an input stimulus, but instead spiking oscillates in the range 20–40 Hz with amplitude at-the-limits. In certain of these cases, such as a preliminary cortical lesion experiment, oscillations were reduced and eventually eliminated following a conclusion of the standard 25-cycle refinement procedure. In this particular case, somatotopy was maintained (though with reduced cortical magnification as the same input layer was driving a smaller cortical network.) In other cases, whether temporal pathologies are observed, or not, the topographic map becomes “degenerate”: three to four representational zones emerge with exceptionally high cortical magnification of a few restricted zones on the input layer, and at times including double-digit receptive fields (even where the input stimulation patterns were single-digit only).

Finally, as with much of cortical neural network modeling, correspondence is most easily drawn with a salient feature of cortical neuroanatomy—the cortical column. While it is possible to observe complex and meaningful spatial-temporal dynamics in these lumped cortical column models, the present results do not explicitly take into account feed-forward and feed-back mechanisms involving sub-cortical contributions (Jones, 2000; Haider et al., 2013; Qi et al., 2014).

Relationship to Other Studies

The contribution of the present study is both confirmatory and distinctly novel with respect to neurophysiological and computational studies of cortical columns and cortical neural networks.

Neurophysiology

Allard et al. (1991) demonstrated that temporally correlated afferent input activity plays a role in the emergence and plasticity of receptive fields and representational maps in the primary somatosensory cortex of adult monkeys. These findings are reproduced here through simulated differential use of digits in a model hand. When adjacent input layer patches on opposing digits were driven by temporally correlated stimulation (a direct consequence of simulated digital syndactyly) cortical receptive fields transformed to extend across the line of syndactyly onto the “joined” input layer patches of both fused digits and abolished the digit representational boundary. The model mechanism through which differential use transformed receptive field characteristics and representational topography was the operation of a covariance learning rule on excitatory and inhibitory synapses. The present model provides a framework within which to generate hypotheses to link neurophysiological observations and mechanisms with features of cortical neuroanatomy principally the cortical column.

Initial neurophysiological descriptions of somatosensory cortical columns remarked upon the similarity of receptive field size and overlap (Mountcastle, 1957, 1997). Subsequent studies observed that receptive field extent was smallest in layer IV, with overlapping similar receptive field sizes, or larger to substantially larger receptive field extent in supragranular and infragranular areas (Sur et al., 1985; Chapin, 1986; Haupt et al., 2004). Studies in rat whisker-barrel cortex have demonstrated short latency excitatory response in inhibitory cells (Brumberg et al., 1999; Petersen and Diamond, 2000) and inhibition of excitatory cells (Simons and Carvell, 1989; Brumberg et al., 1996) arising from activation of principal and adjacent whiskers. Studies of *in vitro* adult rat neocortical functional borders have described diverse excitatory and inhibitory outcomes following tetanic stimulation (Hickmott and Merzenich, 2002; Paullus and Hickmott, 2011).

Neuroanatomical contributions to laminar similarities and differences have been attributed to the laminar distribution of cell types and differential input-output patterns. Electrophysiological contributions have been attributed to the interplay between thalamo-cortically driven feed-forward excitation and feed-forward inhibition, recurrent intra- and inter-columnar excitatory and inhibitory circuits, and complex polysynaptic cortico-cortical connections. A possible functional contribution or consequence of receptive field size similarities and differences may reflect differential contributions to general principles of cortical layer IV processing. Miller et al. (2001), noted common organizing principles in a comparative analysis of cat primary visual cortex (V1) and the whisker-barrel fields of rodent primary somatosensory cortex with respect to response sharpening of excitatory cells and enhancement of response to effective stimuli. An additional possible role has been discussed with respect to modulating excitability and preventing hyperexcitability (Sun et al., 2006; Benali et al., 2008).

The present results are unique in generating novel hypotheses for neurophysiological testing. The results focus on observable laminar differences in receptive field size in neurophysiological recording tracks oriented perpendicular to the pial surface (e.g., cortical columns) in adult monkey area 3b and rat SI cortex. The experimental protocol might proceed to implement

a standard receptive field mapping protocol to analyze adjacent cortical representations that each have sufficiently high cortical magnification and sufficiently small layer IV excitatory receptive field sizes. Such conditions may be met in the cortical representation of the glabrous skin surface of the phalanges of adjacent fingers of the hand in the monkey, or at the face-forearm representation in the rat. By sufficiently high cortical magnification is meant a representation that is large enough to support identification of a “within-representational” zone distant from all representational discontinuities. By sufficiently extensive representational borders is meant a region of discontinuity that permits multiple penetrations along and on both sides of the discontinuity. And by sufficiently small within-representational layer IV excitatory receptive field sizes is meant that increases in excitatory (inhibitory) receptive field size within- and between recording penetrations should be readily and obviously detectable using standard receptive field mapping procedures.

The present model predicts that with the above protocol the data should, in their simplest form, yield two characteristic, statistically significantly different, laminar difference profiles. One profile will correspond to the “within-representation” type (e.g., type WR) and the other will be the “boundary-adjacent” type (e.g., type BA). Furthermore, subject to experimental manipulation of the type described in this study, the experimenter will be able to cause reversible change from type BA to type WR, and from type WR to type BA. A variation on the above hypothesis is to induce plasticity in a representational discontinuity contemporaneously with single-unit or multi-unit recordings of both excitatory and inhibitory cells and taking into account laminar position.

Computational Studies

The present computational model shares features in common with the literature of distributed self-organizing neural networks (Wilson and Cowan, 1972, 1973; von der Malsburg, 1973; Freeman, 1975; Willshaw and von der Malsburg, 1976; Takeuchi and Amari, 1979; Kohonen, 1982; Oja, 1982; Grajski and Merzenich, 1990; Joubin et al., 1996; Eglén and Gjorgjieva, 2009; Detorakis and Rougier, 2012, 2014; Harris and Mrsic-Flogel, 2013) which may be considered as a subclass (winner-take-all networks) of general models of unsupervised learning networks (Binas et al., 2014). The robustness of the results reported above in response to variations of the particular covariance rule was confirmed by varying connection strength relaxation time constant (α_w), the weight adaptation step size (β_w), the weight adaptation step size relaxation time constant (α_β), and normalization frequency (i.e., per time-step vs per trial). Anecdotally, the formation of topographic maps with representational discontinuities was most sensitive to the weight adaptation step size (β_w). Excitatory receptive field organization was more sensitive than inhibitory receptive field organization. For example, with much larger values than those listed in **Table 1E** (e.g., $>10x$), while inhibitory receptive field centroids distributed as reported, excitatory receptive field centroids organized in a degenerate fashion (see Section Limitations and extensions). The dependence of reported results on additional variations of the simple covariance rule (e.g., connection weight constraints other than normalization) or more complex

dependencies (e.g., spike timing-dependence, Vogels et al., 2013; Kleberg et al., 2014) has not been explored.

The present computational model differs from and extends previous results in several ways. First, afferent and lateral network connectivity details are not assigned *a priori*. In prior studies it is not unusual to find that afferent connection strengths are modeled *a priori* as arising from a localized Gaussian distribution. This is distinct from assignment of spatial filtering of input so as to model skin effects. In the present case, afferent connection strengths are drawn from a uniform distribution. With respect to lateral connectivity, prior studies may define a parameterized lateral connectivity pattern in order to effect lateral inhibition. The present study initializes local lateral connection strengths from a uniform distribution. Second, network dynamics are simply those that evolve as given by the network equations with no additional higher order operations to select maximum responses or otherwise affect the time evolution of the network. Third, a quite simple covariance rule is applied to drive synaptic plasticity on **all** connections of the network, in particular inhibitory plasticity. In prior studies it is not unusual that only certain classes of connections are plastic and subject to a range from simple to complex adaptation rules. Fourth, detailed analysis of somatotopy, receptive field size and cortical magnification are provided separately for the component excitatory and inhibitory cell populations. Fifth, the experimental simulation protocol is designed to isolate a specific experimentally observed phenomenon (cortical representational discontinuity and its reorganization) so that its neural mechanism can be compared and contrasted with controls at the level of the evolution of spatial patterns by type of individual synaptic connections strengths. Finally, the present study suggests that perhaps there are additional features of neural networks that may be understood as fundamentally emergent.

Future Directions

This author is aware of few studies, until quite recently, comparable with the present study in which there is synaptic plasticity on all connections and, in particular, inhibitory synaptic plasticity (Grajski and Merzenich, 1990; Vogels et al., 2013; Binas et al., 2014; Kleberg et al., 2014). Present results establish a foundation for further numerical studies. How does the hand representation reorganize in response to targeted “silencing” or “amplification” of combinations of local cortical population subtypes? How does reorganization compare between within-representation and boundary-adjacent representational zones? Can the present model framework be extended to better relate features of cortical maps and their reorganization to sensation and the recovery of sensation in the clinical neurology of the hand?

The modeling study reported here may have potential application in personalized medicine analogous to that described for The Virtual Brain project (Leon et al., 2013; Falcon et al., 2016). Specifically, primary somatosensory cortical plasticity following release from syndactyly has been observed in adult humans (Mogilner et al., 1993; Stavrinou et al., 2007).

Stavrinou et al., observed correlates of reorganization over the course of a roughly 6 h long preparation during which artificial syndactyly was imposed and released. Mogilner et al., observed reorganization of primary somatosensory cortical hand representation in two patients following surgical separation of webbed fingers. The degree of reorganization correlated with the severity of syndactyly. For one patient, reorganization yielded somatotopy and nearly normal representational area. For the second patient, though reorganization yielded distinct cortical locations for digits, the representational area was smaller than normal and nonsomatopic. Could the present modeling framework, simulation protocol and measurements combined with individualized clinical data be combined to predict post-surgical cortical reorganizational outcomes? Could these predicted outcomes, in turn, be applied to predict extent and progression of recovery of sensation in the hand? Several extensions to the present hand model could potentially lead to clinically meaningful results. First, select one or more clinical assessments or psychophysical tasks (localization, two-point discrimination, vibratory sense) as behavioral touchstones (Dellon, 1981). Second, select a mechanoreceptor class or classes and skin surface model corresponding to the selected behavioral task (Zimmerman et al., 2014). Last, tailor model input layer, output layer and input stimulation pattern parameters through the translation of individual area 3b finger representation neuroanatomical and functional details (van Westen et al., 2004). Combined with the experimental protocol described in this paper, these extensions could generate model cortical reorganizational correlates of behavioral task performance under syndactyly, release from syndactyly, and potentially to other hand-related peripheral and central injuries.

SOFTWARE AND DATA

Author-generated research (e.g., not for commercial use) C++ simulation code and R analysis scripts used to generate the Figures in this paper have been placed in a *GitHub* repository: <https://github.com/kgrajski/KamilGrajski-Somatopic-Discontinuity-Plasticity/>.

AUTHOR CONTRIBUTIONS

The author confirms being the sole contributor of this work and approved it for publication.

FUNDING

This work was entirely self-funded.

ACKNOWLEDGMENTS

The author gratefully acknowledges reviewers' comments, and the encouragement of Dr. Dean V. Buonomano, Dr. Peter Hickmott, and Dr. Michael Merzenich.

REFERENCES

- Allard, T., Clark, S. A., Jenkins, W. M., and Merzenich, M. M. (1991). Reorganization of somatosensory area 3b representations in adult owl monkeys after digital syndactyly. *J. Neurophys.* 66, 1048–1058.
- Benali, A., Weiler, E., Benali, Y., Dinse, H. R., and Eysel, U. T. (2008). Excitation and inhibition jointly regulate cortical reorganization in adult rats. *J. Neurosci.* 28, 12284–12293. doi: 10.1523/JNEUROSCI.1952-08.2008
- Binas, J., Ruthishauser, U., Indiveri, G., and Pfeiffer, M. (2014). Learning and stabilization of winner-take-all dynamics through interacting excitatory and inhibitory plasticity. *Front. Comput. Neurosci.* 8:68. doi: 10.3389/fncom.2014.00068
- Brumberg, J. C., Pinto, D. J., and Simons, D. J. (1996). Spatial gradients and inhibitory summation in the rat whisker barrel system. *J. Neurophysiol.* 76, 130–140.
- Brumberg, J. C., Pinto, D. J., and Simons, D. J. (1999). Cortical columnar processing in the rat whisker-to-barrel system. *J. Neurophysiol.* 82, 1808–1817.
- Chapin, J. K. (1986). Laminar differences in sizes, shapes and response profiles of cutaneous receptive fields in the rat SI cortex. *Exp. Brain Res.* 62, 549–5559.
- Dellon, A. L. (1981). *Evaluation of Sensibility and Re-education of Sensation in the Hand*. Baltimore: Williams & Wilkins.
- Detorakis, G. I., and Rougier, N. P. (2012). A neural field model of the somatosensory cortex: formation, maintenance and reorganization or ordered topographic maps. *PLoS ONE* 7:e40257. doi: 10.1371/journal.pone.0040257
- Detorakis, G. I., and Rougier, N. P. (2014). Structure of receptive fields in a computational model of area 3b of primary sensory cortex. *Front. Comput. Neurosci.* 8:76. doi: 10.3389/fncom.2014.00076
- DiCarlo, J. J., and Johnson, K. O. (2002). Receptive field structure in cortical area 3b of the alert monkey. *Behav. Brain Res.* 135, 167–178.
- Dicarlo, J. J., Johnson, K. O., and Hsiao, S. S. (1998). Structure of receptive fields in area 3b of primary somatosensory cortex in the alert monkey. *J. Neurosci.* 18, 2626–2645.
- Eglen, S. J., and Gjorgjieva, J. (2009). Self-organization in the developing nervous system: theoretical models. *Hfsp J.* 3, 176–185. doi: 10.2976/1.3079539
- Falcon, M. I., Jirsa, V., and Solodkin, A. (2016). A new neuroinformatics approach to personalized medicine in neurology: the Virtual Brain. *Curr. Opin. Neurol.* 29, 429–436. doi: 10.1097/WCO.0000000000000344
- Freeman, W. J. (1975). *Mass Action in the Nervous System*. Cambridge, MA: Academic Press.
- Goodhill, G. J., and Sejnowski, T. J. (1996). Quantifying neighbourhood preservation in topographic mappings. In *Proceeding of 3rd Joint Symposium Neurol Comp. Vol. 6* (La Jolla, CA), 61–82.
- Grajski, K. A., and Merzenich, M. (1990). Hebb-type dynamics is sufficient to account for the inverse magnification rule in cortical somatotopy. *Neural Comput.* 2, 71–84.
- Haider, B., Hausser, M., and Carandini, M. (2013). Inhibition dominates sensory responses in the awake cortex. *Nature* 493, 97–102. doi:10.1038/nature11665
- Harris, K. D., and Mrsic-Flogel, T. D. (2013). Cortical connectivity and sensory coding. *Nature* 503, 51–58. doi:10.1038/nature12654
- Haupt, S. S., Spengler, F., Husemann, R., and Dinse, H. R. (2004). Receptive field scatter, topography and map variability in different layers of the hindpaw representation of rat somatosensory cortex. *Exp. Brain Res.* 155, 485–499. doi: 10.1007/s00221-003-1755-3
- Hickmott, P. W., and Merzenich, M. M. (2002). Local circuit properties underlying cortical reorganization. *J. Neurophysiol.* 88, 1288–1301. doi: 10.1152/jn.00994.2001
- Jones, E. G. (2000). Cortical and subcortical contributions to activity-dependent plasticity in primate somatosensory cortex. *Annu. Rev. Neurosci.* 23, 1–57. doi: 10.1146/annurev.neuro.23.1.1
- Joublin, F., Spengler, F., Wacquant, S., and Dinse, H. R. (1996). A columnar model of somatosensory reorganizational plasticity based on Hebbian and non-Hebbian learning rules. *Biol. Cybern.* 74, 275–86.
- Kaas, J. H., Nelson, R., Sur, M., Lin, C. S., and Merzenich, M. M. (1979). Multiple representations of the body within the primary somatosensory cortex of primates. *Science* 204, 521–523.
- Kleberg, F. I., Fukai, T., and Gilson, M. (2014). Excitatory and inhibitory STDP jointly tune feedforward neural circuits to selectively propagate correlated spiking activity. *Front. Comput. Neurosci.* 8:53. doi: 10.3389/fncom.2014.00053
- Kohonen, T. (1982). Self-organized formation of topographically correct feature maps. *Biol. Cybern.* 43, 59–69.
- Leon, P. S., Knock, S. A., Woodman, M. M., Domide, L., Mersmann, J., McIntosh, A. R., et al. (2013). The Virtual Brain: a simulator of primate brain network dynamics. *Front. Neuroinform.* 7:00010. doi: 10.3389/fninf.2013.00010
- Merzenich, M. M., Kaas, J. H., Sur, M., and Lin, C. S. (1978). Double representation of the body surface within cytoarchitectonic areas 3b and 1 in S1 in the owl monkey (*Aotus trivirgatus*). *J. Comp. Neurol.* 181, 41–73.
- Merzenich, M. M., Nelson, R. J., Kaas, J. H., Stryker, M. P., Jenkins, W. M., Zook, J. M., et al. (1987). Variability in hand surface representations in areas 3b and 1 in adult owl and squirrel monkeys. *J. Comp. Neurol.* 258, 281–296.
- Merzenich, M., Recanzone, G. H., Jenkins, W. M., and Grajski, K. A., (1990). Adaptive mechanisms in cortical networks underlying cortical contributions to learning and nondeclarative memory. *Cold Spring Harb. Symp. Quant. Biol.* 55, 873–87.
- Miller, K. D., Pinto, D. J., and Simons, D. J. (2001). Processing in layer 4 of the neocortical circuit: new insights from visual and somatosensory cortex. *Curr. Opin. Neurobiol.* 11, 488–497.
- Mogilner, A., Grossman, J. A., Ribary, U., Joliot, M., Volkmann, J., Rapaport, D., et al. (1993). Somatosensory cortical plasticity in adult humans revealed by magnetoencephalography. *Proc. Natl. Acad. Sci. U.S.A.* 90, 3593–3597.
- Mountcastle, V. B. (1957). Modality and topographic properties of single neurons of cat's somatic sensory cortex. *J. Neurophysiol.* 20, 408–434.
- Mountcastle, V. B. (1997). The columnar organization of the neocortex. *Brain* 120, 701–722.
- Nordlie, E., Gewaltig, M.-O., and Plesser, H. E. (2009). Towards reproducible descriptions of neuronal network models. *PLoS Comput. Bio.* 5:e1000456. doi:10.1371/journal.pcbi.1000456.
- Oja, E. (1982). A simplified neuron model as a principal components analyzer. *J. Math. Biol.* 15, 267–273.
- Paullus, J. R., and Hickmott, P. W. (2011). Diverse excitatory and inhibitory synaptic plasticity outcomes in complex horizontal circuits near a functional border of adult neocortex. *Brain Res.* 1416, 10–25. doi: 10.1016/j.brainres.2011.07.062
- Petersen, R. S., and Diamond, M. E. (2000). Spatial-temporal distribution of whisker-evoked activity in the rat somatosensory cortex and the coding of stimulus location. *J. Neurosci.* 20, 6135–6143.
- Qi, H. X., Kass, J. H., and Reed, J. L. (2014). The reactivation of somatosensory cortex and behavioral recovery after sensory loss in mature primates. *Front. Syst. Neurosci.* 8:84. doi: 10.3389/fnsys.2014.00084
- Recanzone, G. H., Merzenich, M. M., Jenkins, W. M., Grajski, K. A., and Dinse, H. R. (1992). Topographic reorganization of the hand representation in cortical area 3b of owl monkeys trained in a frequency-discrimination task. *J. Neurophys.* 67, 1031–1056.
- Simons, D. J., and Carvell, G. E. (1989). Thalamocortical response transformation in the rat vibrissa/barrel system. *J. Neurophysiol.* 61, 311–330.
- Stavrinou, M. L., Della Penna, S., Pizzella, V., Torquati, K., Cianflone, F., Franciotti, R., et al. (2007). Temporal dynamics of plastic changes in human primary somatosensory cortex after finger webbing. *Cereb. Cortex* 17, 2134–2142. doi: 10.1093/cercor/bhl120
- Sun, Q., Huguenard, J. R., and Prince, D. A. (2006). Barrel cortex microcircuits: thalamocortical feedforward inhibition in spiny stellate cell is mediated by a small number of fast-spiking interneurons. *J. Neurosci.* 26, 1219–1230. doi: 10.1523/JNEUROSCI.4727-04.2006
- Sur, M. (1980). Receptive fields of neurons in areas 3b and 1 of somatosensory cortex in monkeys. *Brain Res.* 198, 465–471.
- Sur, M., Garraghty, P. E., and Bruce, C. J. (1985). Somatosensory cortex in macaque monkeys: laminar differences in receptive field size in areas 3b and 1. *Brain Res.* 342, 391–395.
- Sur, M., Merzhehich, M. M., and Kaas, J. H. (1980). Magnification, receptive field area, and “hypercolumn” size in areas 3b and 1 of somatosensory cortex in owl monkeys. *J. Neurophysiol.* 44, 295–311.
- Takeuchi, A., and Amari, S. (1979). Formation of topographic maps and columnar microstructures in nerve fields. *Biol. Cybern.* 35, 63–72.
- van Westen, D., Fransson, P., Olsrud, J., Rosén, B., Lundborg, G., and Larsson, E. M., (2004). Fingersomatopy in area 3b: an fMRI study. *BMC Neurosci.* 5:28. doi:10.1186/1471-2202-5-28

- Vogels, T. P., Froemke, R. C., Doyon, N., Gilson, M., Haas, J. S., Liu, R., et al. (2013). Inhibitory synaptic plasticity: spike timing-dependence and putative network function. *Front. Neural Circuits* 7:119. doi: 10.3389/fncir.2013.00119
- von der Malsburg, C. (1973). Self-organization of orientation sensitive cells in the striate cortex. *Kybernetik* 14, 85–100.
- Willshaw, D. J., and von der Malsburg, C. (1976). How patterned neural connections can be set up by self-organization. *Proc. R. Soc. Lond. B* 194, 431–445.
- Wilson, H. R., and Cowan, J. D. (1972). Interactions in localized populations of model neurons. *Biophys. J.* 12, 1–24.
- Wilson, H. R., and Cowan, J. D. (1973). A mathematical theory of the functional dynamics of cortical and thalamic nervous tissue. *Kybernetik* 13, 55–80.
- Zimmerman, A., Bai, L., and Ginty, D. D. (2014). The gentle touch receptors of mammalian skin. *Science* 346, 950–954.

Conflict of Interest Statement: The authors declare that the research was conducted in the absence of any commercial or financial relationships that could be construed as a potential conflict of interest.

Copyright © 2016 Grajski. This is an open-access article distributed under the terms of the Creative Commons Attribution License (CC BY). The use, distribution or reproduction in other forums is permitted, provided the original author(s) or licensor are credited and that the original publication in this journal is cited, in accordance with accepted academic practice. No use, distribution or reproduction is permitted which does not comply with these terms.